Combined Connectomics, *MAPT* Gene Expression, and Amyloid Deposition to Explain Regional Tau Deposition in Alzheimer Disease

Lukai Zheng, MD, MMed [1] Anna Rubinski, PhD,[1] Jannis Denecke, MSc [1]

Ying Luan, MD, PhD,[1,2] Ruben Smith, MD, PhD,[3] Olof Strandberg, PhD,[3]

Erik Stomrud, MD, PhD,[3,4] Rik Ossenkoppele, PhD,[3,5,6] Diana Otero Svaldi, PhD,[7]

Ixavier Alonzo Higgins, PhD,[7] Sergey Shcherbinin, PhD,[7] Michael J. Pontecorvo, PhD,[7,8]

Oskar Hansson, MD, PhD [3,4] Nicolai Franzmeier, PhD [1,9,10] and Michael Ewers, PhD, [1,11]

for the Alzheimer's Disease Neuroimaging Initiative

Objective: We aimed to test whether region-specific factors, including spatial expression patterns of the tau-encoding gene *MAPT* and regional levels of amyloid positron emission tomography (PET), enhance connectivity-based modeling of the spatial variability in tau-PET deposition in the Alzheimer disease (AD) spectrum.

Methods: We included 685 participants (395 amyloid-positive participants within AD spectrum and 290 amyloid-negative controls) with tau-PET and amyloid-PET from 3 studies (Alzheimer's Disease Neuroimaging Initiative, ^{18}F-AV-1451-A05, and BioFINDER-1). Resting-state functional magnetic resonance imaging was obtained in healthy controls (n = 1,000) from the Human Connectome Project, and *MAPT* gene expression from the Allen Human Brain Atlas. Based on a brain-parcellation atlas superimposed onto all modalities, we obtained region of interest (ROI)-to-ROI functional connectivity, ROI-level PET values, and *MAPT* gene expression. In stepwise regression analyses, we tested connectivity, *MAPT* gene expression, and amyloid-PET as predictors of group-averaged and individual tau-PET ROI values in amyloid-positive participants.

Results: Connectivity alone explained 21.8 to 39.2% (range across 3 studies) of the variance in tau-PET ROI values averaged across amyloid-positive participants. Stepwise addition of *MAPT* gene expression and amyloid-PET increased the proportion of explained variance to 30.2 to 46.0% and 45.0 to 49.9%, respectively. Similarly, for the prediction of patient-level tau-PET ROI values, combining all 3 predictors significantly improved the variability explained

(mean adjusted R^2 range across studies = 0.118–0.148, 0.156–0.196, and 0.251–0.333 for connectivity alone, connectivity plus *MAPT* expression, and all 3 modalities combined, respectively).

Interpretation: Across 3 study samples, combining the functional connectome and molecular properties substantially enhanced the explanatory power compared to single modalities, providing a valuable tool to explain regional susceptibility to tau deposition in AD.

Neurofibrillary tau tangles (NFTs) constitute a core pathology of Alzheimer disease (AD) and are closely correlated with neurodegeneration and cognitive decline.[1] During the course of the disease, NFTs typically emerge in circumscribed brain areas, including the entorhinal cortex, and subsequently progress to other cortical brain areas.[2] However, the regional patterns of tau deposition differ substantially between subjects at a given level of disease severity,[3,4] which contributes to the heterogeneity in cognitive and clinical symptoms in AD.[5,6] Therefore, it is of great clinical value to understand which factors influence the spatial differences in tau accumulation in AD.

One major potential source that influences the spatial distribution of tau deposition in the brain is the connectivity between brain regions.[3] Multiple lines of evidence have suggested that pathologic tau trans-synaptically propagates between neurons in vitro,[7] and spreads along axonal connections in the brain of transgenic mouse models of tauopathy,[8] consistent with the hypothesis of a prionlike spreading of fibrillar tau between interconnected regions.[9] In humans, the assessment of transaxonal transfer cannot be measured directly at the system level. However, functional and structural connectomes of large-scale networks can be employed to assess connectivity between brain regions in humans as a predictor of the spatial progression of tau between brain regions. Based on the combination of the normative human functional connectome and positron emission tomography (PET) scans of fibrillar tau in patients of AD, we and others have previously shown that higher connectivity of tau epicenters (assumed to reflect the earliest tau-affected regions) is predictive of higher tau accumulation in the connected region,[3,10] consistent with the view that fibrillar tau progresses from initial seed regions preferentially to closely connected brain regions. Despite these encouraging results, a substantial portion of variability in the spatial patterns of tau deposition remained unexplained,[3,10] prompting urgent research needs to advance patient-level explanation of regional patterns of tau deposition.

Here, we propose combining functional connectivity and markers of local vulnerability to enhance the explanation of region-specific susceptibility to fibrillar tau. Our approach was motivated by previous findings suggesting that region-specific cellular properties such as differences in gene expression[11,12] and the presence of other major pathologies including cortical amyloid deposition[13] may influence regional tau accumulation in AD. For gene expression, recent results from human transcriptomics suggest that the normative brain expression patterns of specific genes spatially resemble predilection areas of tau pathology.[14] Specifically, the expression pattern of the gene called microtubule-associated protein tau (*MAPT*) strongly resembled the spatial patterns of tau-PET spreading and gray matter atrophy.[11,14] Because *MAPT* encodes the tau protein, which serves as the substrate for NFTs, brain regions with high *MAPT* expression may be particularly prone to develop NFTs in AD. In terms of the influence of regional amyloid-beta (Aβ) deposition on tau accumulation, the Aβ protein was previously reported to facilitate the formation of fibrillar tau in transgenic mouse models of Aβ and tau pathology.[15,16] In humans, cortical fibrillar tau is almost exclusively found in the presence of abnormally elevated levels of Aβ in cortical brain areas as measured by PET imaging,[17,18] suggesting that regional cortical Aβ facilitates the spread of tau from medial temporal to connected neocortical brain areas.[13] Therefore, regional variability in the severity of amyloid-PET accumulation may contribute to the regional heterogeneity in the spreading of tau pathology in AD. Whereas higher connectivity to epicenter may contribute to explaining the tau spreading between different regions, the accumulation of tau in the connected region may be facilitated by local Aβ levels.[13] Yet, despite the evidence supporting the contribution of such local factors to regional tau susceptibility in the brain, robust multimodal modeling that integrates regional molecular properties and interregional connectivity for explaining tau-PET accumulation patterns is still lacking.

Here, we addressed that research gap by combining the functional connectome, normative transcriptomic brain maps of *MAPT* expression, and individual measurements of regional Aβ deposition to explain regional susceptibility to tau-PET deposition. We tested the models in 3 different samples of patients with biomarker evidence of AD to assess the robustness of our findings. Overall, we provide a framework to leverage both regional factors and connectivity and thereby present a powerful approach toward precision medicine-guided explanation of tau-PET deposition patterns at the patient level in AD.

Subjects and Methods

Participants

Alzheimer's Disease Neuroimaging Initiative. We included 410 participants encompassing 279 cognitively normal (CN) subjects, 80 subjects with mild cognitive impairment (MCI), and 51 subjects with AD dementia from the Alzheimer's Disease Neuroimaging Initiative (ADNI) study (NCT01231971 and NCT02854033).[19] A detailed description of the ADNI study can be found in the ADNI General Procedures Manual.[20] In addition to the inclusion criteria of ADNI,[21] selection criteria for our study included the availability of ^{18}F-flortaucipir PET (to assess fibrillar tau) and ^{18}F-florbetapir PET (to assess Aβ deposition) spaced no longer than 6 months apart. The clinical classification of CN, MCI, or dementia was assessed by ADNI investigators as previously described.[21] Briefly, the criteria for CN were the absence of major depression, Mini-Mental State Examination (MMSE) score ≥ 24, and Clinical Dementia Rating (CDR) = 0; for MCI, objective memory loss on education-adjusted Wechsler Memory Scale II, preserved activities of daily living, MMSE ≥ 24, and CDR = 0.5; and for AD dementia, fulfillment of the National Institute of Neurological and Communicative Disorders and Stroke–Alzheimer's Disease and Related Disorders Association (NINCDS-ADRDA) probable AD criteria,[22] MMSE ≤ 26, and CDR > 0.5. Beyond the above criteria, we excluded participants with non-AD-related (ie, amyloid-negative [Aβ⁻]) cognitive impairment.

Ethical approval was obtained by the ADNI investigators. All participants provided written informed consent.

^{18}F-AV-1451-A05. A total of 220 participants comprising 67 CN subjects, 85 MCI patients, and 68 participants with dementia were included from the ^{18}F-AV-1451-A05 study (henceforth referred to as "A05"; NCT02016560), which is a completed observational trial to assess the association between ^{18}F-flortaucipir uptake and subsequent cognitive decline.[23] In addition to the inclusion criteria of A05,[23] other criteria included the availability of ^{18}F-florbetapir PET obtained at baseline (within 2 months from the ^{18}F-flortaucipir PET scan). The classification criteria for CN subjects were MMSE ≥ 29 and no history of cognitive impairment; for MCI subjects, 24 ≤ MMSE ≤ 29 and fulfillment of the 2011 National Institute on Aging/Alzheimer's Association (NIA-AA) MCI criteria[24]; and for dementia patients, 10 < MMSE < 24, and fulfillment of the 2011 NIA-AA possible or probable AD criteria.[25] Similar to ADNI, we further excluded participants with non-AD-related cognitive impairment (determined as Aβ⁻ MCI and Aβ⁻ dementia).

The A05 study was approved by the relevant institutional review boards, and all participants signed informed consent.[26]

Swedish BioFINDER-1. We included 55 participants, encompassing 30 CN, 7 MCI, and 18 dementia cases from the Swedish BioFINDER-1 cohort (NCT01208675).[27] In addition to the inclusion criteria of BioFINDER-1,[27] further requirements were the availability of ^{18}F-flutemetamol PET (to assess Aβ deposition) and ^{18}F-flortaucipir PET. The classification criteria for CN were MMSE ≥ 28 and no measurable cognitive deficits on a neuropsychological battery examining verbal, visuospatial, episodic memory, and executive functions[28]; for MCI, MMSE ≥ 24 and objective memory loss on the above neuropsychological battery; and for dementia, fulfillment of the Diagnostic and Statistical Manual of Mental Disorders (third edition, revised) dementia criteria,[29] as well as the NINCDS-ADRDA probable AD criteria. Furthermore, we excluded participants classified as Aβ⁻ MCI and Aβ⁻ dementia.

The BioFINDER-1 study was approved by the regional ethical review board in Lund, Sweden. Participants gave their written informed consent to participate.

Image Acquisition and Processing

Alzheimer's Disease Neuroimaging Initiative. Structural magnetic resonance imaging (MRI) data were acquired on 3T scanners using 3-dimensional T1-weighted magnetization-prepared rapid acquisition gradient echo (MPRAGE) sequences with 1mm isotropic resolution and a repetition time (TR)/echo time (TE) of 3,000/30 milliseconds. ^{18}F-flortaucipir PET was acquired using 6 × 5-minute frames from 75 to 105 minutes after injection of 370MBq of the tracer. Amyloid-PET was acquired in 4 × 5-minute frames, 50 to 70 minutes after injection of ^{18}F-florbetapir (370MBq). The standardized imaging acquisition protocol for ADNI can be found online.[30]

For each participant, the T1 magnetic resonance (MR) images were segmented and the high-dimensional spatial normalization parameters for registration to the Montreal Neurological Institute (MNI) 152 space[31] were estimated using the Advanced Normalization Tools (ANTs) cortical-thickness pipeline (see Tustison et al[32] for a detailed description). The parameters were subsequently applied to each participant's corresponding ^{18}F-flortaucipir and ^{18}F-florbetapir PET scans for registration to MNI space. The thus registered ^{18}F-flortaucipir PET scans were intensity-normalized, using the inferior cerebellar cortex as the reference region,[33] and the regional standardized uptake value ratios (SUVRs) were extracted for 200 cortical regions of interest (ROIs) based on the Schaefer atlas.[34] Finally, the ROI values of ^{18}F-flortaucipir SUVRs were

converted into z scores (henceforth called ^{18}F-flortaucipir z scores) based on the data from the Aβ⁻ CN reference group for each specific ROI.[35] This involved transforming each participant's ROI value by subtracting the average ROI value of the reference group and then dividing it by the standard deviation of the reference group's ROI values. For ^{18}F-florbetapir PET scans, the registered images were intensity-normalized to the mean signal in the whole cerebellum, and the global ^{18}F-florbetapir SUVRs were calculated as the average SUVR of frontal, anterior/posterior cingulate, lateral parietal, and lateral temporal regions according to a previously described protocol.[36,37] The Aβ status was determined based on established cut-points of global ^{18}F-florbetapir SUVR > 1.11.[30] We also extracted regional mean ^{18}F-florbetapir SUVRs for 200 Schaefer ROIs and calculated ^{18}F-florbetapir z scores using the ^{18}F-florbetapir PET scans from the Aβ⁻ CN group as reference data.

^{18}F-AV-1451-A05. Structural MRI data were acquired across multiple scanners (1.5 or 3T) using volumetric T1-weighted sequences. ^{18}F-flortaucipir PET was acquired using 4 × 5-minute frames from 80 to 100 minutes after injection of 370MBq of the tracer. Amyloid-PET was acquired in 2 × 5-minute frames, 50 to 60 minutes after injection of ^{18}F-florbetapir (370MBq). A detailed description of imaging acquisition in A05 was given elsewhere.[23]

All MR and PET images were processed as previously described.[23] Briefly, structural T1 MR images were segmented into tissue compartments using Statistical Parametric Mapping (SPM) and spatially normalized to the MNI space using FMRIB's nonlinear image registration tool (FNIRT).[38] The derived spatial normalization parameters were applied to the coregistered ^{18}F-flortaucipir PET scans, which were subsequently intensity-normalized to the inferior cerebellar gray as the reference region. For the ^{18}F-florbetapir PET data, summed motion-corrected scans were spatially normalized to a ^{18}F-florbetapir PET template in MNI space using nonlinear registration methods in SPM and subsequently intensity-normalized using the whole cerebellum as the reference region. All ^{18}F-florbetapir PET images were visually interpreted by experienced Avid investigators and classified by consensus as Aβ⁻ or Aβ⁺.[23] Readers had access to regional and global average quantitative PET scan information, which was used as an adjunct to the visual read.[23] Regional mean SUVRs were extracted for 200 Schaefer ROIs for both the ^{18}F-flortaucipir and ^{18}F-florbetapir PET scans, followed by the conversion of these values into z scores referenced to the Aβ⁻ CN group.

BioFINDER-1. For all BioFINDER-1 participants, structural MRI data were acquired on 3T scanners using T1-weighted MPRAGE (1mm isotropic resolution, TR/TE = 1,900/2.64 milliseconds) sequences. Tau-PET was acquired 80 to 100 minutes after injection of ^{18}F-flortaucipir, whereas amyloid-PET was acquired 90 to 110 minutes after injection of ^{18}F-flutemetamol. A detailed description of MRI and PET data acquisition in BioFINDER-1 can be found elsewhere.[39]

All MR and PET images were processed centrally by the BioFINDER imaging core in Lund.[40] In brief, T1 MR images were segmented via FreeSurfer,[41] and high-dimensional spatial normalization parameters were estimated using ANTs.[40] Attenuation- and motion-corrected ^{18}F-flortaucipir and ^{18}F-flutemetamol PET images were intensity-normalized to the inferior cerebellar gray matter as the reference region for ^{18}F-flortaucipir PET images and to the pons for the ^{18}F-flutemetamol PET images, and subsequently normalized to MNI space by applying the T1-derived transformation parameters. Global ^{18}F-flutemetamol SUVR was defined as an average SUVR across prefrontal, parietal, temporal lateral, anterior cingulate, posterior cingulate, and precuneus cortices.[42] A previously defined cutoff (global ^{18}F-flutemetamol SUVR > 0.575) was applied to determine Aβ status.[43] Regional SUVRs of each PET image were also extracted for 200 Schaefer ROIs and then converted into z scores referenced to the Aβ⁻ CN group.

Identification of Tau Epicenters

Following a previously developed approach,[3] we determined tau epicenters for each Aβ⁺ participant, defined as those ROIs that show the highest ^{18}F-flortaucipir z scores among the 200 ROIs within a given participant. The number of epicenters was kept constant across all Aβ⁺ participants. The optimal number of epicenters was defined based on the maximal R^2 value of epicenter–connectivity distance to explain the ^{18}F-flortaucipir deposition at a given number of epicenter ROIs in the ADNI sample. To this end, we first averaged all ^{18}F-flortaucipir z score maps across the Aβ⁺ participants and ranked the ROIs in descending order of the group-averaged ROI values of ^{18}F-flortaucipir z scores in the ADNI sample. Next, we systematically varied the number of ROIs as candidate epicenters (ranging from top 1 to top 30 ROIs of highest ^{18}F-flortaucipir z score, increasing by steps of 1). For each number of ROIs, the R^2 value of the connectivity-based prediction of the ROI levels of ^{18}F-flortaucipir z scores was determined. The number 5 ROIs yielded the highest R^2, which also gained high model performance in the other two datasets. Finally, we determined for each participant the tau epicenters as the 5 highest ranking ROIs within the participant's ^{18}F-flortaucipir z score map.

Functional Connectivity Template and Connectivity Distance

We computed pairwise functional connectivity for all ROI pairs in the 200-ROI Schaefer atlas using the resting state functional MRI (fMRI) scans from 1,000 healthy participants recruited within the Human Connectome Project (HCP), as described previously.[3] Briefly, minimally preprocessed 3T resting-state fMRI images (spatially normalized to MNI space; for details see Smith et al[44]) were downloaded from the HCP database, and further processed by detrending, bandpass filtering (0.01–0.08Hz), despiking, and motion correction. As an additional measure to control for motion artifacts, frames with displacement > 0.5mm were scrubbed along with 1 preceding and 2 subsequent frames. Based on the processed fMRI images, we extracted regional-average time course within each of the 200 ROIs and assessed Pearson moment correlations of the time courses for each pair of ROIs, resulting in participant-level functional connectivity matrices. The correlation coefficients were Fisher z-transformed and averaged across participants to create a group-level connectivity matrix.

For the computation of connectivity distance (ie, the length of the shortest path connecting two ROIs in the functional network),[45] we retained 70% of the strongest positive connections within the group-level connectivity matrix to eliminate weak and potentially noisy connections.[3] Connectivity distance was computed for each pair of ROIs using Floyd's algorithm,[46] resulting in a distance matrix. Floyd's distance is defined as the shortest distance between two nodes in a graph, where the edges are weighted by the connectivity. Epicenter–connectivity distance of an ROI was defined as the average connectivity distance of a target ROI to all 5 epicenter ROIs for a given participant.

Spatial Maps of MAPT Gene Expression

For our hypothesis-driven analysis focusing on *MAPT* gene expression, the spatial gene expression data of *MAPT* were derived from mRNA profiling of 6 healthy human brains in the Allen Human Brain Atlas (AHBA).[47] Specifically, we used a whole-brain gene expression map, where the *MAPT* mRNA levels were interpolated at all locations throughout the brain in MNI standard space as described previously.[48] In brief, mRNA microarray data obtained from AHBA were symmetrized across hemispheres, filtered, and averaged across probes, mean-centering normalized across donors, and finally fitted into a variogram model to predict mRNA level for each voxel in MNI space. Several probe filtering methods were applied, including intensity-based filtering of background signal (>1%), correlation-based filtering of probes (Pearson $r > 0.3$), and a stepwise selection based on spatial variability of the variogram modeling.[48]

Based on the whole-brain map, we computed the average *MAPT* gene expression level in each of the 200 ROIs from the Schaefer atlas. To this end, we created a gray matter mask (thresholded at the probability of >0.3) from the segmented T1 scans in the ADNI sample and superimposed the mask onto the *MAPT* gene expression map to obtain the ROI expression values.

Statistical Analysis

All statistical analyzes were performed with R version 4.2.0 (www.R-project.org). First, we tested whether the spatial similarity between the *MAPT* gene expression and group-average ^{18}F-flortaucipir z scores in corresponding ROIs was exceptionally high among the 18,686 gene expression maps of protein-encoding genes mapped in the AHBA.[48] To this end, we computed for each gene the spatial correlation (Pearson correlation coefficient) at the ROI level between gene expression ROI levels and the average ^{18}F-flortaucipir z score ROI levels among Aβ+ participants, rendering a sampling distribution of the spatial correlation coefficients across genes. We determined the percentile rank of the spatial correlation coefficient for the *MAPT* gene within the sampling distribution. Additionally, we extended this analysis by narrowing down the gene pool to include only those genes labeled as brain-elevated genes (n = 2,098) in the Human Protein Atlas.[49] These brain-elevated genes show at least 4-fold higher expression in the brain compared to other organs and tissues, thus providing a more stringent reference for assessing the spatial similarity to ^{18}F-flortaucipir deposition. To control for spatial autocorrelation, the significance (p_{spin}) of the correlation between ^{18}F-florbetapir z scores and *MAPT* expression was established against 10,000 spatial permutations using Vasa's method, which is an implementation of the nonparametric spin test for parcellated brain map.[50]

Next, to replicate our previous findings that shorter epicenter–connectivity distance was associated with higher ^{18}F-flortaucipir z scores in the connected ROIs,[3] we performed linear regression with group-average ROI values of ^{18}F-flortaucipir z scores as the dependent variable and epicenter–connectivity distance as the independent variable within the Aβ+ group. To test our hypothesis that regional *MAPT* expression and amyloid-PET z scores enhance connectivity-based prediction of ^{18}F-flortaucipir z scores, we added in a stepwise manner the terms *MAPT* expression and amyloid-PET z scores (all at the ROI level) to the initial connectivity-only model. The explanatory power of the above models was assessed by adjusted R^2 values (R^2_{adj}) and compared between the models by likelihood ratio tests. To account for spatial autocorrelation, we also performed 10,000 spatial permutations per modality (epicenter–connectivity distance/*MAPT* expression/amyloid-PET) and assessed the significance (p_{spin}) of R^2_{adj} against a null distribution of R^2_{adj} derived from the permuted maps.

For participant-level analyses, the above-described regression analyzes were repeated for each Aβ+ participant separately. To this end, the tau epicenters (5 ROIs with the highest ^{18}F-flortaucipir z score) were determined for each participant separately, and the epicenter–connectivity distance was calculated accordingly on the HCP-derived connectivity matrix. R^2_{adj} values of the models were compared with paired t tests across participants within each sample.

Results

Sample Characteristics

Basic demographic and clinical characteristics are summarized by diagnostic group and study in Table 1. The

TABLE 1. Demographic and Basic Participant Characteristics

ADNI, N = 410	Aβ⁻ CN, n = 211	Aβ⁻ CN, n = 68	Aβ⁻ MCI, n = 80	AD dementia, n = 51	p
Age, yr	73.3 ± 7.5	77.0 ± 7.1	76.3 ± 7.5	78.6 ± 8.9	<0.001
Male, n (%)	95 (45.0)	25 (36.8)	47 (58.8)	28 (54.9)	0.031
Education, yr	17 ± 3	17 ± 2	16 ± 3	15 ± 2	0.001
MMSE	29.0 ± 1.2	28.83 ± 1.4	26.93 ± 2.3	21.9 ± 4.6	<0.001
ADAS-13	8.18 ± 4.16	9.04 ± 5.32	17.80 ± 6.89	31.00 ± 9.83	<0.001
APOE-ε4, n (%)[a]	59 (29.4)	34 (51.5)	47 (61.8)	30 (60.0)	<0.001
A05, N = 220	**Aβ⁻ CN, n = 63**	**Aβ⁻ CN, n = 4**	**Aβ⁻ MCI, n = 85**	**AD dementia, n = 68**	***p***
Age, yr	58.5 ± 19.7	78.1 ± 8.0	74.5 ± 9.2	75.0 ± 9.66	<0.001
Male, n (%)	36 (57.1)	3 (75.0)	49 (57.6)	32 (47.1)	0.451
Education, n (%)					0.554
≥13 years	54 (85.7)	4 (100.0)	66 (77.6)	55 (80.9)	-
Otherwise	9 (14.3)	0 (0)	19 (22.4)	13 (19.1)	-
MMSE	29.4 ± 0.8	28.8 ± 1.9	25.6 ± 3.2	22.0 ± 10.5	<0.001
ADAS-11	5.29 ± 3.26	5.75 ± 3.95	13.7 ± 5.84	22.0 ± 10.5	<0.001
APOE-ε4, n (%)	13 (21.0)	1 (25.0)	44 (52.4)	42 (64.6)	<0.001
BioFINDER-1, N = 55	**Aβ⁻ CN, n = 16**	**Aβ⁻ CN, n = 14**	**Aβ⁻ MCI, n = 7**	**AD dementia, n = 18**	***p***
Age, yr	73.9 ± 5.3	76.2 ± 5.0	72.7 ± 6.6	69.8 ± 10.5	0.126
Male, n (%)	10 (62.5)	6 (42.9)	2 (28.6)	11 (61.1)	0.357
Education, yr	13 ± 4	11 ± 3	11 ± 3	13 ± 3	0.118
MMSE	29.0 ± 1.1	29.2 ± 1.1	25.6 ± 2.9	22.1 ± 5.2	<0.001
ADAS-delayed recall	1.81 ± 1.47	2.29 ± 1.59	6.17 ± 2.40	7.62 ± 2.45	<0.001
APOE-ε4, n (%)	0 (0)	8 (57.1)	4 (57.1)	11 (61.1)	<0.001

Note: Values are n (%) for categorical variables and mean ± standard deviation for continuous variables; p values are derived from χ^2 tests for categorical variables, and analyses of variance for continuous variables.

[a]Proportion of *APOE-ε4* carriers was based on individuals who had information on *APOE* genotype, which was available for 393 of 410 participants in the ADNI sample, 215 of 220 participants in the A05 sample, and all the participants in the BioFINDER-1 sample.

Abbreviations: A05 = ¹⁸F-AV-1451-A05; AD = Alzheimer disease; ADAS = Alzheimer's Disease Assessment Scale; ADNI = Alzheimer's Disease Neuroimaging Initiative; Aβ = amyloid-beta; CN = cognitively normal; MCI = mild cognitive impairment; MMSE = Mini-Mental State Examination.

group-average maps of cortical ¹⁸F-flortaucipir SUVRs in the Aβ⁺ groups are shown for all 3 samples in Figure 1A. Higher ¹⁸F-flortaucipir z scores (>3) were observed on average primarily in the temporal lobe and medial posterior parietal cortex for each of the 3 studies (see Supplementary Fig S1 for average ¹⁸F-flortaucipir z score maps split by clinical group within each study). The *MAPT* expression was primarily observed in the posterior parietal,

lateral temporal, entorhinal, precuneus, and cingulate cortex (see Fig 1B).

Spatial Similarity between Flortaucipir z Scores and *MAPT* Expression

Higher regional *MAPT* expression was associated with higher ¹⁸F-flortaucipir z scores across spatially corresponding ROIs within the Aβ⁺ group (ADNI: $r = 0.375$, $p_{spin} = 0.004$;
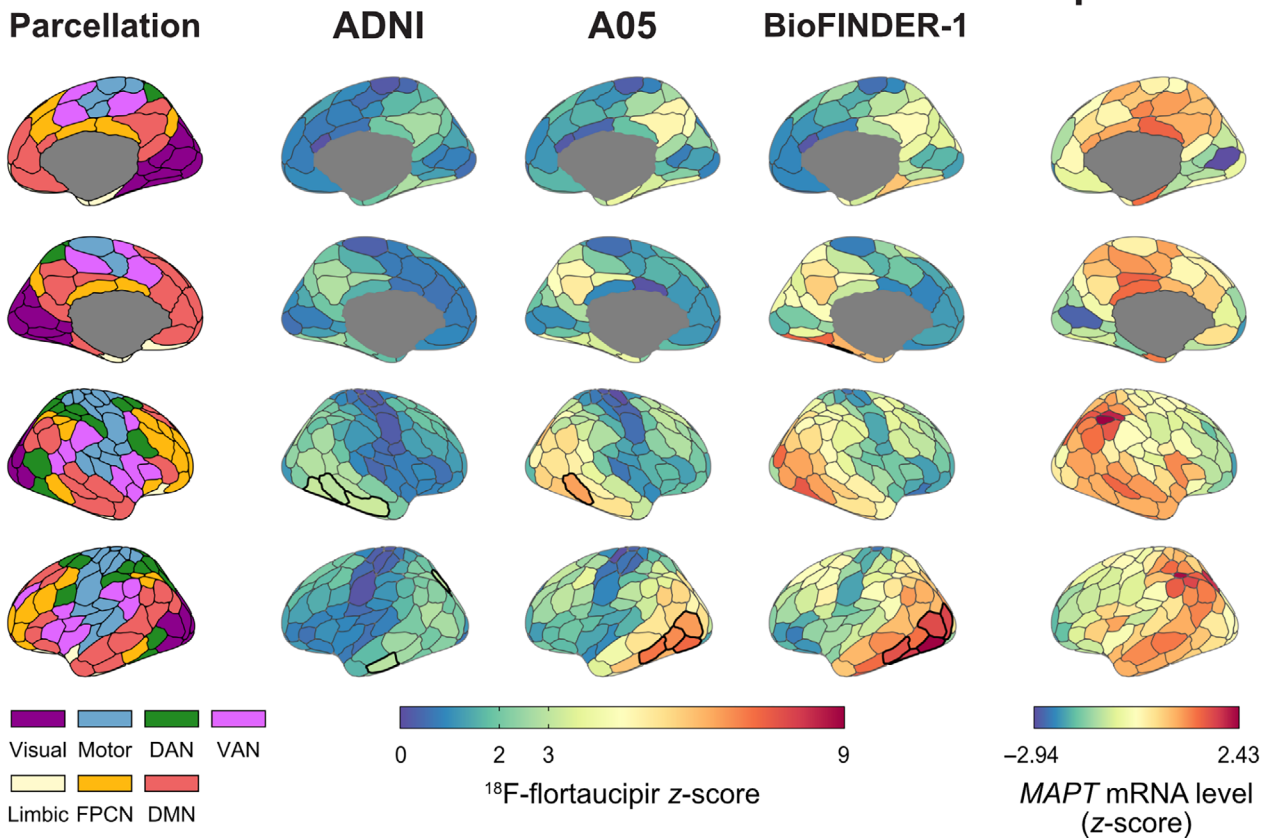
FIGURE 1: Spatial distribution of ^{18}F-flortaucipir deposition and *MAPT* expression. (A) Surface rendering of the ^{18}F-flortaucipir *z* scores within regions of interest (ROIs) defined by a 200-ROI brain parcellation atlas (first column; resting-state functional networks are color-coded) applied to ^{18}F-flortaucipir PET scans from Aβ$^+$ participants in each study. (B) Average *MAPT* gene expression in spatially corresponding ROIs. Tau epicenter ROIs are displayed in bold colors. A05 = ^{18}F-AV-1451-A05; ADNI = Alzheimer's Disease Neuroimaging Initiative; DAN = dorsal attention network; DMN = default mode network; FPCN = frontoparietal control network; PET = positron emission tomography; VAN = ventral attention network.

A05: $r = 0.371$, $p_{spin} = 0.019$; BioFINDER-1: $r = 0.386$, $p_{spin} = 0.024$). To test whether the spatial correlation between ^{18}F-flortaucipir *z* scores and *MAPT* stands out against that between tau and the expression of other genes in the brain, we computed the distribution of spatial correlations between group-averaged ^{18}F-flortaucipir maps of Aβ$^+$ participants and the spatial expression of each of the 18,686 genes in the AHBA atlas. The correlation scores for ^{18}F-flortaucipir versus *MAPT* ranked between the top 2rd and 3th percentile when compared to those between the ^{18}F-flortaucipir *z* scores and the expression of any other of the 18,686 genes in the AHBA atlas (ADNI: top 2th percentile; A05: top 2th percentile; BioFINDER1: top 3th percentile; Fig 2), confirming a higher spatial match between ^{18}F-flortaucipir *z* scores and *MAPT* expression when compared to most other genes in the AHBA across study samples. Furthermore, we replicated this analysis in a subset of genes that are highly expressed in the brain (n = 2,098).

The percentile rank of the correlation between *MAPT* gene expression and ^{18}F-flortaucipir *z* scores remained high compared to that of most other genes (ADNI: top 5th percentile; A05: top 5th percentile; BioFINDER-1: top 5th percentile; Supplementary Fig S2).

MAPT Expression and Amyloid-PET for Explaining Interregional Tau Variation at the Group Level within the Aβ$^+$ Group

First, we replicated our previous findings of the association between epicenter–connectivity distance and ^{18}F-flortaucipir *z* scores in the connected brain regions in each of the 3 samples of Aβ$^+$ participants (Table 2, Fig 3A).[3,51] Overall, shorter epicenter–connectivity distance was associated with higher average ^{18}F-flortaucipir *z* scores in the connected ROIs, with $R^2_{adj} = 0.392$ (in ADNI study), 0.218 (A05), and 0.221 (BioFINDER-1) within the Aβ$^+$ participants (ADNI: $p_{spin} < 0.001$; A05: $p_{spin} < 0.001$; BioFINDER-1:
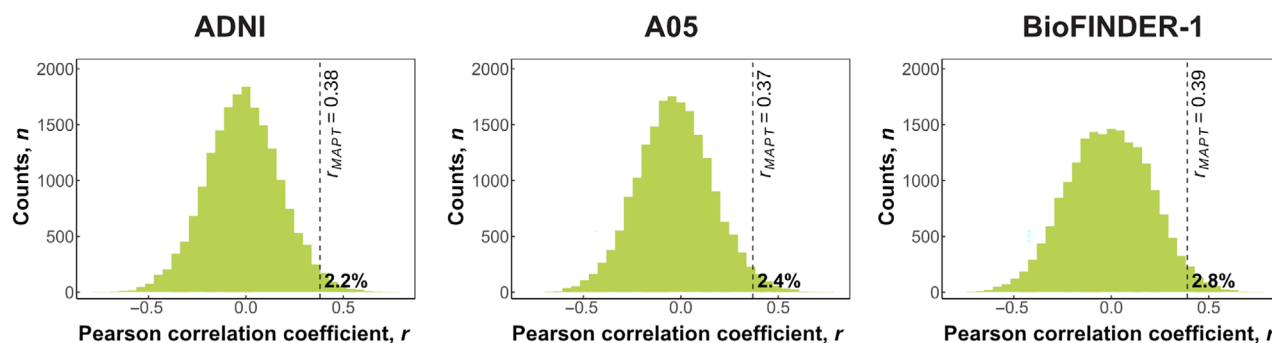
FIGURE 2: Association between ^{18}F-flortaucipir and gene expression across 18,686 genes. The vertical dotted lines indicate the percentiles of the correlation coefficients for the associations between *MAPT* gene expression versus ^{18}F-flortaucipir *z* scores for each of the 3 studies. A05 = ^{18}F-AV-1451-A05; ADNI = Alzheimer's Disease Neuroimaging Initiative.

$p_{spin} = 0.013$), confirming our previous findings that epicenter–connectivity distance partially explains the inter-regional variability in tau-PET deposition in AD.[3,51] When adding *MAPT* expression to the epicenter–connectivity distance for the prediction of regional ^{18}F-flortaucipir *z* score, the combined model led to a significant improvement by 7 to 12% in explanatory power (connectivity-only model vs 2-predictor combined model, ADNI: $R^2_{adj} = 0.392$ vs 0.460, $p < 0.001$; A05: $R^2_{adj} = 0.218$ vs 0.302, $p < 0.001$; BioFINDER-1: $R^2_{adj} = 0.221$ vs 0.343, $p < 0.001$). In contrast, *MAPT* expression alone explained only 11.5%/13.6%/15.7% of the variance in ADNI/A05/BioFINDER-1 samples (ADNI: $p_{spin} = 0.010$; A05: $p_{spin} = 0.010$; BioFINDER-1: $p_{spin} = 0.008$).

In a final step, we tested whether adding amyloid-PET *z* scores as a third independent variable further enhanced the explanatory power. Compared to the reduced model (epicenter–connectivity distance plus *MAPT* expression), the addition of amyloid-PET *z* scores as a predictor variable increased the proportion of explained variance by an additional 2 to 20% (ADNI: $R^2_{adj} = 0.460$ vs 0.479, $p = 0.005$; A05: $R^2_{adj} = 0.302$ vs 0.499, $p < 0.001$; BioFINDER-1: $R^2_{adj} = 0.343$ vs 0.450, $p < 0.001$). These results suggest that both regional *MAPT* expression levels and participant-level amyloid-PET *z* scores in a given ROI enhance the epicenter–connectivity distance model to explain regional ^{18}F-flortaucipir *z* scores.

We conducted sensitivity analyzes in clinically defined subgroups of Aβ$^+$ participants in ADNI and A05 (note that we did not attempt subgroup analysis in the BioFINDER-1 sample and the Aβ$^+$ CN subgroup of A05 due to smaller sample size). The above intermodel differences remained in the Aβ$^+$ MCI and AD dementia participants, but not the Aβ$^+$ CN group (Supplementary Fig S3). Specifically, regional *MAPT* expression did not explain the group-averaged ROI values of ^{18}F-flortaucipir

z scores in the Aβ$^+$ CN group ($R^2_{adj} = 0.037$, $p_{spin} = 0.092$), potentially due to the low-level, spatially restricted ^{18}F-flortaucipir deposition in that group.

Participant-Level Analysis of ^{18}F-Flortaucipir PET Prediction

Based on previous findings explaining the group-average spatial pattern of ^{18}F-flortaucipir *z* scores in the Aβ$^+$ participants, we next asked whether the model also explains the spatial variability in the individual tau-PET deposition. Therefore, we repeated the analysis, this time testing the models to explain ^{18}F-flortaucipir *z* scores at the participant level. Consistent with the previous analysis reported above based on group-average ^{18}F-flortaucipir *z* scores, adding *MAPT* expression to epicenter–connectivity distance led to an increase in the proportion of explained variability in participant-level tau *z* scores (connectivity-only model vs 2-predictor combined model, ADNI: mean $R^2_{adj} = 0.118$ vs 0.156, $p < 0.001$; A05: mean $R^2_{adj} = 0.148$ vs 0.196, $p < 0.001$; BioFINDER-1: mean $R^2_{adj} = 0.119$ vs 0.162, $p < 0.001$; see Table 2, Fig 4). Adding amyloid-PET *z* scores increased the proportion of explained variance in ^{18}F-flortaucipir *z* scores by an additional 8 to 15% (ADNI: mean $R^2_{adj} = 0.156$ vs 0.333, $p < 0.001$; A05: mean $R^2_{adj} = 0.196$ vs 0.282, $p < 0.001$; BioFINDER-1: mean $R^2_{adj} = 0.162$ vs 0.251, $p < 0.001$). Sensitivity analysis in clinically defined subgroups showed enhanced explanatory value of the full models (including *MAPT* expression and amyloid-PET) in each of the clinical subgroups within Aβ$^+$ participants (Supplementary Fig S4).

Discussion

Our main finding was that the spatial patterns of *MAPT* expression and regional amyloid-PET *z* scores enhanced the epicenter–connectivity distance-based model for explaining spatial ^{18}F-flortaucipir patterns in AD. We reproduced these findings across samples from 3 studies,

TABLE 2. Regression Models to Predict Group-Averaged and Participant-Level ^{18}F-Flortaucipir SUVRs

Statistical model	ADNI		A05		BioFINDER-1	
	β (95% CI)	R^2_{adj} (95% CI)	β (95% CI)	R^2_{adj} (95% CI)	β (95% CI)	R^2_{adj} (95% CI)
Group-averaged ^{18}F-flortaucipir PET						
Model A		0.392 (0.282 to 0.495)		0.218 (0.122 to 0.324)		0.221 (0.124 to 0.327)
Epicenter–connectivity distance	−0.629 (−0.739 to −0.518)		−0.471 (−0.597 to −0.346)		−0.474 (−0.599 to −0.349)	
Model B		0.115 (0.043 to 0.208)		0.136 (0.057 to 0.233)		0.157 (0.073 to 0.258)
Regional *MAPT* expression	0.345 (0.212 to 0.479)		0.374 (0.243 to 0.506)		0.402 (0.272 to 0.532)	
Model C		0.460 (0.349 to 0.555)		0.302 (0.192 to 0.406)		0.343 (0.231 to 0.446)
Epicenter–connectivity distance	−0.593 (−0.698 to −0.488)		−0.418 (−0.538 to −0.297)		−0.437 (−0.552 to −0.321)	
Regional *MAPT* expression	0.268 (0.163 to 0.373)		0.300 (0.179 to 0.420)		0.356 (0.241 to 0.472)	
Model D		0.479 (0.365 to 0.570)		0.499 (0.387 to 0.588)		0.450 (0.335 to 0.543)
Epicenter–connectivity distance	−0.562 (−0.667 to −0.456)		−0.472 (−0.574 to −0.369)		−0.484 (−0.591 to −0.377)	
Regional *MAPT* expression	0.252 (0.148 to 0.355)		0.302 (0.200 to 0.404)		0.297 (0.190 to 0.405)	
Regional amyloid	0.150 (0.045 to 0.256)		0.448 (0.347 to 0.549)		0.337 (0.230 to 0.445)	
Participant-level ^{18}F-flortaucipir PET[a]						
Model A		0.118 (0.101 to 0.134)		0.148 (0.127 to 0.169)		0.119 (0.085 to 0.152)
Epicenter–connectivity distance	−0.304 (−0.328 to −0.280)		−0.345 (−0.374 to −0.316)		−0.313 (−0.365 to −0.262)	
Model B		0.043 (0.036 to 0.050)		0.058 (0.049 to 0.068)		0.051 (0.034 to 0.068)
Regional *MAPT* expression	0.106 (0.079 to 0.132)		0.203 (0.181 to 0.227)		0.189 (0.143 to 0.236)	
Model C		0.156 (0.137 to 0.174)		0.196 (0.173 to 0.220)		0.162 (0.122 to 0.202)
Epicenter–connectivity distance	−0.296 (−0.320 to −0.272)		−0.332 (−0.360 to −0.303)		−0.301 (−0.353 to −0.250)	
Regional *MAPT* expression	0.092 (0.066 to 0.117)		0.180 (0.157 to 0.202)		0.167 (0.121 to 0.213)	
Model D		0.333 (0.313 to 0.354)		0.282 (0.260 to 0.304)		0.251 (0.204 to 0.298)
Epicenter–connectivity distance	−0.216 (−0.244 to −0.189)		−0.308 (−0.338 to −0.279)		−0.275 (−0.329 to −0.221)	
Regional *MAPT* expression	0.092 (0.069 to 0.116)		0.183 (0.161 to 0.205)		0.137 (0.085 to 0.190)	
Regional amyloid	0.417 (0.390 to 0.444)		0.260 (0.234 to 0.286)		0.225 (0.150 to 0.299)	

[a]For the participant-level regression models, the β and R^2_{adj} averaged across participants and their 95% CI are presented.

Abbreviations: A05 = ^{18}F-AV-1451-A05; ADNI = Alzheimer's Disease Neuroimaging Initiative; CI = confidence interval; PET = positron emission tomography; R^2_{adj} = adjusted proportion variance explained; β = standardized regression coefficient.
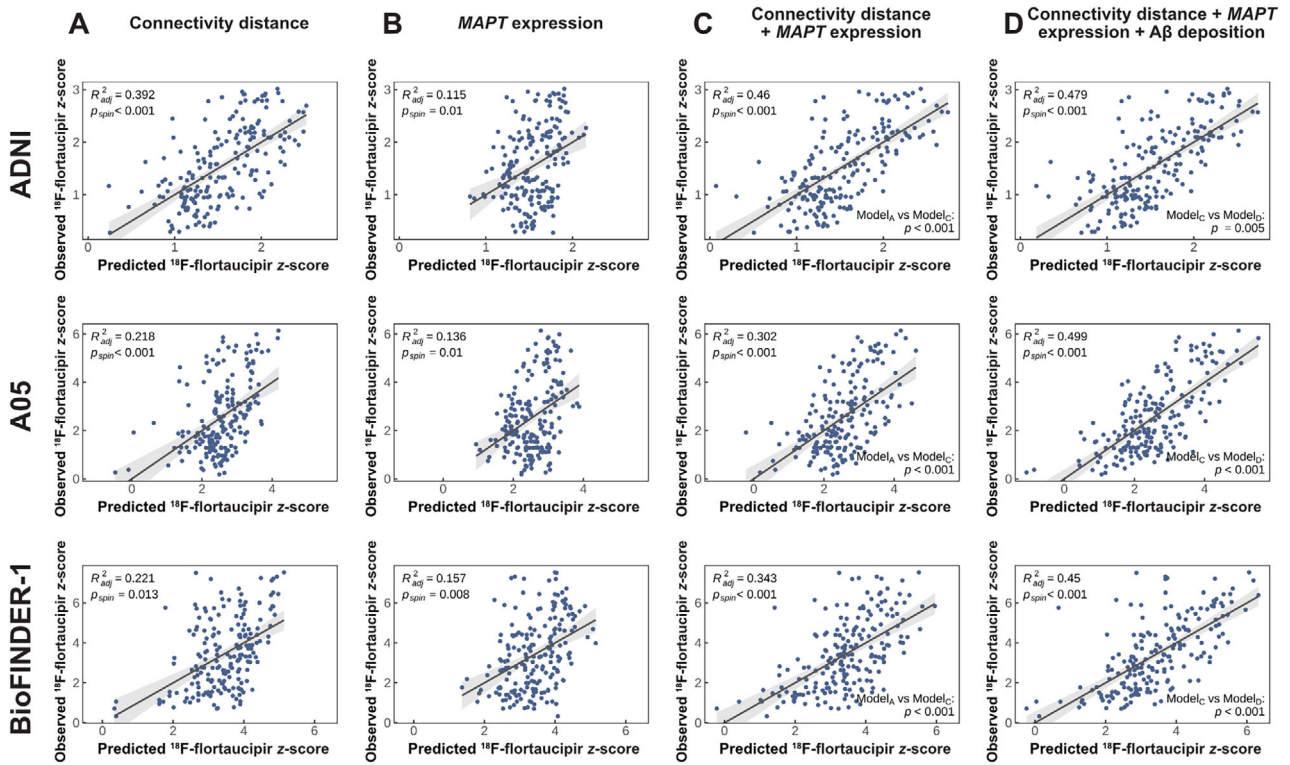
FIGURE 3: Prediction of group-average ^{18}F-flortaucipir z scores. Regression plots show the association between the predicted versus observed ^{18}F-flortaucipir z scores for each regression model including connectivity only (A), *MAPT* expression only (B), connectivity plus *MAPT* expression (C), and all 3 modalities combined (D). A05 = ^{18}F-AV-1451-A05; ADNI = Alzheimer's Disease Neuroimaging Initiative; Aβ = amyloid-beta; p_{spin} = spatial autocorrelation-corrected p value for spin-based permutation testing; R^2_{adj} = adjusted proportion variance explained.
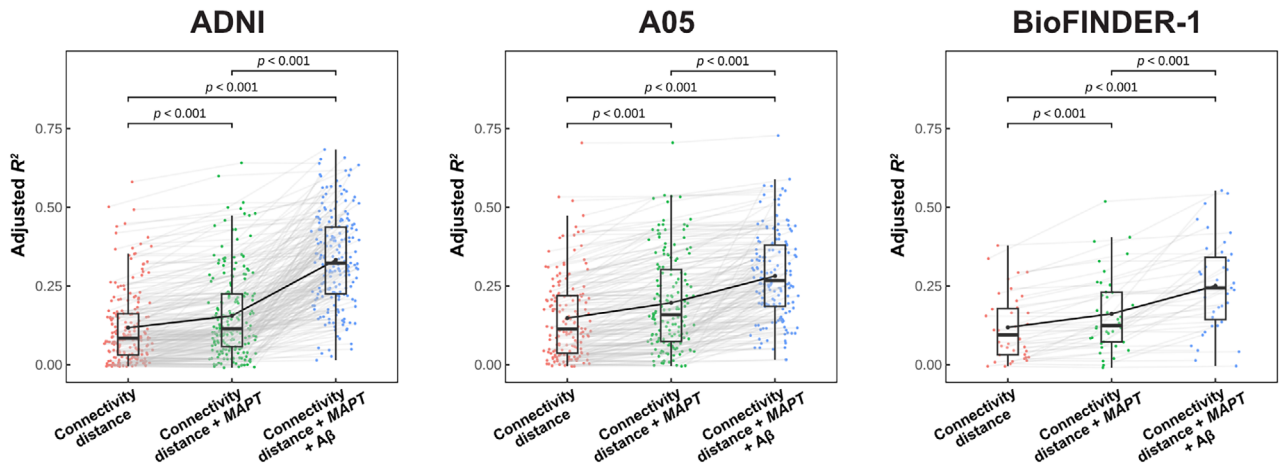
FIGURE 4: Prediction of participant-level ^{18}F-flortaucipir z scores. Box plots show the distribution of adjusted R^2 values for each regression model including connectivity-only models (*red dots*), connectivity plus *MAPT* expression (*green dots*), and all 3 modalities combined (*blue dots*) for each study. The R^2 values were compared between models using paired t tests. A05 = ^{18}F-AV-1451-A05; ADNI = Alzheimer's Disease Neuroimaging Initiative; Aβ = amyloid-beta.

suggesting a robust benefit of our multimodal model over connectivity for the prediction of ^{18}F-flortaucipir z scores in patients with biomarker evidence of AD. Our findings advance the results of previous studies to explain regional patterns of tau pathology.[3,10] Compared to connectivity-only

models, the introduction of local gene expression and individual-level amyloid-PET increased the explained proportion of variance by 9 to 28% to a total of 45 to 50% across 3 samples, demonstrating a substantial benefit of the integrated multimodal model compared to

previous results. Toward precision medicine, we also performed a patient-level modeling of regional tau-PET deposition in addition to the group-level analysis. This is a more difficult task, as individual patterns in ^{18}F-flortaucipir z scores vary more than the group average. Our results showed a slightly reduced explanatory value for patient-level compared to group-level ^{18}F-flortaucipir z scores, but still demonstrated a significant increase in the effect size of the fully integrated prediction model compared to reduced models. Our approach, therefore, provides an important step forward to identify the factors that may underlie regional susceptibility to tau accumulation and yields a framework to build an integrated multidimensional model of regional tau-PET deposition applicable at the individual level in AD.

For the gene expression mapping, we focused, in a hypothesis-driven manner, on *MAPT* among more than 18,000 protein-encoding genes mapped in the AHBA. Our focus on the *MAPT* gene was driven by previous findings of a spatial match of regional *MAPT* gene expression and trajectories of tau spreading in the brain.[11] Supporting those previous findings, we found that *MAPT* gene expression showed a spatial association with tau-PET deposition surpassing the top 5th percentile among all genes mapped in the AHBA and when considering only those protein-encoding genes exhibiting enhanced expression in the brain. A potential mechanisms that may link *MAPT* expression with regional tau pathology is that higher *MAPT* transcript levels are associated with higher regional levels of soluble tau,[52] which may undergo fibrillization and transsynaptic spreading in disease.[7,8] In line with this, we recently found that increased levels of soluble tau are strongly associated with greater tau spread and accumulation over time in early AD.[53] We caution, however, that the proposed pathomechanistic model of tau spreading remains to be demonstrated in future studies.

In addition to *MAPT* expression levels, we found that regional amyloid-PET assessed in each participant was associated with higher regional tau-PET in spatially corresponding ROIs, suggesting that higher regional amyloid-PET adds to the explanation of regional tau PET levels. This finding may at first be surprising, given the spatial divergence of predilected brain areas of amyloid plaques (ie, the default mode network)[54] and tau (ie, medial temporal lobe, locus coeruleus).[2] However, the progression of tau pathology from medial temporal to higher cortical areas (Braak stage III–IV) is typically not seen in the absence of amyloid plaques,[55,56] suggesting that accumulation of fibrillar tau in higher cortical brain areas is facilitated by the presence of amyloid pathology.[13] Converging evidence comes from studies in transgenic animal models of Aβ and pathologic tau, where the spreading of tau from the entorhinal cortex to other cortical brain areas is dramatically enhanced in the presence of cortical Aβ.[57] Our findings are consistent with these previous findings, suggesting an association between regional amyloid-PET levels and tau-PET deposition in AD.

Some caveats should be considered for the interpretation of the current results. First, we focused in the current study on explaining regional variance in tau-PET accumulation averaged across subjects in one of our major analyses. However, previous studies suggest the predominance of spatial subtypes of fibrillar tau spreading in AD, such as the limbic-only or hippocampal sparing subtypes,[4] which we did not take into account. Such subtypes may provide a heuristic for stratified analysis of tau-PET patterns. Rather than stratifying our analysis by tau subtype, we chose to focus on the epicenter-based prediction models. The advantage is that epicenter locations can be individually determined and thus allow for patient-tailored prediction of tau-PET patterns rather than relying on categorical subtyping, where the assignment of individuals to subtypes can be ambiguous. Second, for mapping gene expression, we focused in a hypothesis-driven manner on the *MAPT* gene, but we caution that the expression patterns of *APOE*,[58,59] or other yet-to-be-identified genes, may show similar or even stronger spatial similarity to tau-PET. However, given the large number of potential genes, an exploratory analysis bears the risk of overfitting and would require extensive cross-validation, which was beyond the scope of the current study. Lastly, we employed an out-of-sample functional connectivity template to test our hypothesis that regions typically more strongly connected to tau epicenters exhibit higher tau-PET deposition. However, previous studies have shown that the functional connectome shows interindividual variability[60] that cannot be captured using group-averaged connectivity templates. Furthermore, functional connectivity may change during the disease course,[61] which in turn may influence the progression of tau pathology between connected brain areas. Precision fMRI with extended acquisition times may be particularly suitable to capture idiosyncratic maps of the functional connectome.[62] The current findings encourage future studies using precision fMRI to test whether individual functional connectomes can improve the prediction of AD pathologies beyond the use of connectivity templates.

Overall, our current results demonstrate the additive value of patient-level amyloid-PET scans and atlas-based *MAPT* gene expression mapping to enhance the connectivity-based explanation of tau accumulation. Therefore, the current findings provide important insight into potential sources underlying region-specific

deposition of tau pathology, and encourage future studies to test in patients with AD whether spatial subtypes of amyloid accumulation[63,64] or polymorphisms in tau-related genes are predictive of regional differences in tau deposition and associated domain-specific cognitive impairment.

Author Contributions

M.E. and N.F. contributed to the conception and design of the study. All authors contributed to the acquisition and analysis of data. L.Z., M.E., and N.F. contributed to drafting the manuscript and preparing the figures.

Potential Conflicts of Interest

The ^{18}F-flortaucipir tracer was licensed by Avid Radiopharmaceuticals, a wholly owned subsidiary of Eli Lilly and Company. I.A.H., D.O.S., S.S., and M.J.P. are employees of Eli Lilly and Company. M.E., N.F., and O.H. have received research funding from Eli Lilly and Company. The other authors report no conflicts of interests.

Data Availability

The data can be made available upon reasonable request to the study-specific principal investigator of A05 (Avid Radiopharmaceuticals, a wholly owned subsidiary of Eli Lilly and Company) and BioFINDER-1 (O.H.) or according to the data access stipulations of the open-access data banks of ADNI, AHBA, and HCP.

References

1. Xia C, Makaretz SJ, Caso C, et al. Association of in vivo [18F] AV-1451 tau PET imaging results with cortical atrophy and symptoms in typical and atypical Alzheimer disease. JAMA Neurol 2017;74:427–436.

2. Braak H, Alafuzoff I, Arzberger T, et al. Staging of Alzheimer disease-associated neurofibrillary pathology using paraffin sections and immunocytochemistry. Acta Neuropathol 2006;112:389–404.

3. Franzmeier N, Dewenter A, Frontzkowski L, et al. Patient-centered connectivity-based prediction of tau pathology spread in Alzheimer's disease. Sci Adv 2020;6:eabd1327.

4. Vogel JW, Young AL, Oxtoby NP, et al. Four distinct trajectories of tau deposition identified in Alzheimer's disease. Nat Med 2021;27:871–881.

5. Bejanin A, Schonhaut DR, la Joie R, et al. Tau pathology and neurodegeneration contribute to cognitive impairment in Alzheimer's disease. Brain 2017;140:3286–3300.

6. Brier MR, Gordon B, Friedrichsen K, et al. Tau and Aβ imaging, CSF measures, and cognition in Alzheimer's disease. Sci Transl Med 2016;8:338ra66.

7. Calafate S, Buist A, Miskiewicz K, et al. Synaptic contacts enhance cell-to-cell tau pathology propagation. Cell Rep 2015;11:1176–1183.

8. Clavaguera F, Bolmont T, Crowther RA, et al. Transmission and spreading of tauopathy in transgenic mouse brain. Nat Cell Biol 2009;11:909–913.

9. Mudher A, Colin M, Dujardin S, et al. What is the evidence that tau pathology spreads through prion-like propagation? Acta Neuropathol Commun 2017;5:99.

10. Vogel JW, Iturria-Medina Y, Strandberg OT, et al. Spread of pathological tau proteins through communicating neurons in human Alzheimer's disease. Nat Commun 2020;11:2612.

11. Sepulcre J, Grothe MJ, d'Oleire Uquillas F, et al. Neurogenetic contributions to amyloid beta and tau spreading in the human cortex. Nat Med 2018;24:1910–1918.

12. Montal V, Diez I, Kim C-M, et al. Network tau spreading is vulnerable to the expression gradients of APOE and glutamatergic-related genes. Sci Transl Med 2022;14:eabn7273.

13. Lee WJ, Brown JA, Kim HR, et al. Regional Aβ-tau interactions promote onset and acceleration of Alzheimer's disease tau spreading. Neuron 2022;110:1932–1943.e5.

14. Grothe MJ, Sepulcre J, Gonzalez-Escamilla G, et al. Molecular properties underlying regional vulnerability to Alzheimer's disease pathology. Brain 2018;141:2755–2771.

15. He Z, Guo JL, McBride JD, et al. Amyloid-β plaques enhance Alzheimer's brain tau-seeded pathologies by facilitating neuritic plaque tau aggregation. Nat Med 2018;24:29–38.

16. DeVos SL, Corjuc BT, Commins C, et al. Tau reduction in the presence of amyloid-β prevents tau pathology and neuronal death in vivo. Brain 2018;141:2194–2212.

17. Wang L, Benzinger TL, Su Y, et al. Evaluation of tau imaging in staging Alzheimer disease and revealing interactions between β-amyloid and Tauopathy. JAMA Neurol 2016;73:1070–1077.

18. Ossenkoppele R, Rabinovici GD, Smith R, et al. Discriminative accuracy of [18F]flortaucipir positron emission tomography for Alzheimer disease vs other neurodegenerative disorders. JAMA 2018;320:1151–1162.

19. Weiner MW, Veitch DP, Aisen PS, et al. The Alzheimer's disease neuroimaging initiative 3: continued innovation for clinical trial improvement. Alzheimers Dement 2017;13:561–571.

20. Alzheimer's Disease Neuroimaging Initiative. ADNI General Procedures Manual, Available from: https://adni.loni.usc.edu/wp-content/uploads/2010/09/ADNI_GeneralProceduresManual.pdf.

21. Petersen RC, Aisen PS, Beckett LA, et al. Alzheimer's disease neuroimaging initiative (ADNI): clinical characterization. Neurology 2010;74:201–209.

22. Tierney MC, Fisher RH, Lewis AJ, et al. The NINCDS-ADRDA work group criteria for the clinical diagnosis of probable Alzheimer's disease: a clinicopathologic study of 57 cases. Neurology 1988;38:359.

23. Pontecorvo MJ, Devous MD Sr, Navitsky M, et al. Relationships between flortaucipir PET tau binding and amyloid burden, clinical diagnosis, age and cognition. Brain 2017;140:748–763.

24. Albert MS, DeKosky ST, Dickson D, et al. The diagnosis of mild cognitive impairment due to Alzheimer's disease: recommendations from the National Institute on Aging-Alzheimer's Association workgroups on diagnostic guidelines for Alzheimer's disease. Alzheimers Dement 2011;7:270–279.

25. McKhann GM, Knopman DS, Chertkow H, et al. The diagnosis of dementia due to Alzheimer's disease: recommendations from the National Institute on Aging-Alzheimer's Association workgroups on diagnostic guidelines for Alzheimer's disease. Alzheimers Dement 2011;7:263–269.

26. Pontecorvo MJ, Devous MD, Kennedy I, et al. A multicentre longitudinal study of flortaucipir (18F) in normal ageing, mild cognitive impairment and Alzheimer's disease dementia. Brain 2019;142:1723–1735.

27. Mattsson N, Smith R, Strandberg O, et al. Comparing 18F-AV-1451 with CSF t-tau and p-tau for diagnosis of Alzheimer disease. Neurology 2018;90:e388–e395.

28. Gertje EC, Dv W, Panizo C, et al. Association of Enlarged Perivascular Spaces and Measures of small vessel and Alzheimer disease. Neurology 2021;96:e193–e202.

29. American Psychiatric Association. *Diagnostic and statistical manual of mental disorders (third edition—revised): DSM-III-R.* Washington, DC, USA: Am Psychiatric Assoc, 1987.

30. Alzheimer's Disease Neuroimaging Initiative. ADNI Study Documents, Available from: http://adni.loni.usc.edu/methods/documents.

31. Grabner G, Janke AL, Budge MM, et al. Symmetric atlasing and model based segmentation: an application to the hippocampus in older adults. Med Image Comput Comput Assist Interv 2006;9:58–66.

32. Tustison NJ, Holbrook AJ, Avants BB, et al. The ANTs Longitudinal Cortical Thickness Pipeline2018.

33. Maass A, Landau S, Baker SL, et al. Comparison of multiple tau-PET measures as biomarkers in aging and Alzheimer's disease. Neuroimage 2017;157:448–463.

34. Schaefer A, Kong R, Gordon EM, et al. Local-global Parcellation of the human cerebral cortex from intrinsic functional connectivity MRI. Cereb Cortex 2018;28:3095–3114.

35. Vemuri P, Lowe VJ, Knopman DS, et al. Tau-PET uptake: regional variation in average SUVR and impact of amyloid deposition. Alzheimers Dement (Amst) 2017;6:21–30.

36. Jagust WJ, Landau SM, Koeppe RA, et al. The Alzheimer's disease neuroimaging initiative 2 PET Core: 2015. Alzheimers Dement 2015;11:757–771.

37. Yoon B, Guo T, Provost K, et al. Abnormal tau in amyloid PET negative individuals. Neurobiol Aging 2022;109:125–134.

38. Jenkinson M, Beckmann CF, Behrens TEJ, et al. Fsl. FSL Neuroimage 2012;62:782–790.

39. Smith R, Puschmann A, Schöll M, et al. 18F-AV-1451 tau PET imaging correlates strongly with tau neuropathology in MAPT mutation carriers. Brain 2016;139:2372–2379.

40. Hansson O, Grothe MJ, Strandberg TO, et al. Tau pathology distribution in Alzheimer's disease corresponds differentially to cognition-relevant functional brain networks. Front Neurosci 2017;11:11.

41. Fischl B. FreeSurfer. FreeSurfer NeuroImage 2012;62:774–781.

42. Lundqvist R, Lilja J, Thomas BA, et al. Implementation and validation of an adaptive template registration method for 18F-Flutemetamol imaging data. J Nucl Med 2013;54:1472–1478.

43. Thurfjell L, Lilja J, Lundqvist R, et al. Automated quantification of 18F-Flutemetamol PET activity for categorizing scans as negative or positive for brain amyloid: concordance with visual image reads. J Nucl Med 2014;55:1623–1628.

44. Smith SM, Beckmann CF, Andersson J, et al. Resting-state fMRI in the human connectome project. Neuroimage 2013;80:144–168.

45. Rubinov M, Sporns O. Complex network measures of brain connectivity: uses and interpretations. Neuroimage 2010;52:1059–1069.

46. Floyd RW. Algorithm 97: shortest path. Commun ACM 1962;5:345.

47. Shen EH, Overly CC, Jones AR. The Allen human brain atlas: comprehensive gene expression mapping of the human brain. Trends Neurosci 2012;35:711–714.

48. Gryglewski G, Seiger R, James GM, et al. Spatial analysis and high resolution mapping of the human whole-brain transcriptome for integrative analysis in neuroimaging. Neuroimage 2018;176:259–267.

49. Sjöstedt E, Zhong W, Fagerberg L, et al. An atlas of the protein-coding genes in the human, pig, and mouse brain. Science 2020; 367:eaay5947.

50. Váša F, Seidlitz J, Romero-Garcia R, et al. Adolescent tuning of association cortex in human structural brain networks. Cereb Cortex 2018;28:281–294.

51. Franzmeier N, Rubinski A, Neitzel J, et al. Functional connectivity associated with tau levels in ageing, Alzheimer's, and small vessel disease. Brain 2019;142:1093–1107.

52. Trabzuni D, Wray S, Vandrovcova J, et al. MAPT expression and splicing is differentially regulated by brain region: relation to genotype and implication for tauopathies. Hum Mol Genet 2012;21: 4094–4103.

53. Pichet Binette A, Franzmeier N, Spotorno N, et al. Ayloid-associated increases in soluble tau relate to tau aggregation rates and cognitive decline in early Alzheimer's disease. Nat Commun 2022;13:6635.

54. Palmqvist S, Scholl M, Strandberg O, et al. Earliest accumulation of beta-amyloid occurs within the default-mode network and concurrently affects brain connectivity. Nat Commun 2017;8:1214.

55. Braak H, Braak E. Neuropathological stageing of Alzheimer-related changes. Acta Neuropathol 1991;82:239–259.

56. Sanchez JS, Becker JA, Jacobs HIL, et al. The cortical origin and initial spread of medial temporal tauopathy in Alzheimer's disease assessed with positron emission tomography. Sci Transl Med 2021; 13:eabc0655.

57. Pooler AM, Polydoro M, Maury EA, et al. Amyloid accelerates tau propagation and toxicity in a model of early Alzheimer's disease. Acta Neuropathol Commun 2015;3:14.

58. Dincer A, Chen CD, McKay NS, et al. APOE epsilon4 genotype, amyloid-beta, and sex interact to predict tau in regions of high APOE mRNA expression. Sci Transl Med 2022;14:eabl7646.

59. Ferrari-Souza JP, Lussier FZ, Leffa DT, et al. APOEepsilon4 associates with microglial activation independently of Abeta plaques and tau tangles. Sci Adv 2023;9:eade1474.

60. Gordon EM, Laumann TO, Gilmore AW, et al. Precision functional mapping of individual human brains. Neuron 2017;95:791–807 e7.

61. Badhwar A, Tam A, Dansereau C, et al. Resting-state network dysfunction in Alzheimer's disease: a systematic review and meta-analysis. Alzheimers Dement (Amst) 2017;8:73–85.

62. Gratton C, Laumann TO, Nielsen AN, et al. Functional brain networks are dominated by stable group and individual factors, not cognitive or daily variation. Neuron 2018;98:439–452 e5.

63. Sun Y, Zhao Y, Hu K, et al. Distinct spatiotemporal subtypes of amyloid deposition are associated with diverging disease profiles in cognitively normal and mild cognitive impairment individuals. Transl Psychiatry 2023;13:35.

64. Collij LE, Salvadó G, Wottschel V, et al. Spatial-temporal patterns of beta-amyloid accumulation: a subtype and stage inference model analysis. Neurology 2022;98:e1692–e1703.